Dense nanoimprinted silicon nanowire arrays with passivated axial *p-i-n* junctions for photovoltaic applications

Peng Zhang,[1] Pei Liu,[1] Stylianos Siontas,[1] A. Zaslavsky,[1] D. Pacifici,[1] Jong-Yoon Ha,[2,3] S. Krylyuk,[2,3] and A. V. Davydov[3]
[1]*Department of Physics and School of Engineering, Brown University, Providence, Rhode Island 02912, USA*
[2]*Institute for Research in Electronics and Applied Physics, University of Maryland, College Park, Maryland 20742, USA*
[3]*Material Measurement Laboratory, National Institute of Standards and Technology, Gaithersburg, Maryland 20899, USA*

(Received 16 December 2014; accepted 18 March 2015; published online 31 March 2015)

We report on the fabrication and photovoltaic characteristics of vertical arrays of silicon axial *p-i-n* junction nanowire (NW) solar cells grown by vapor-liquid-solid (VLS) epitaxy. NW surface passivation with silicon dioxide shell is shown to enhance carrier recombination time, open-circuit voltage (V_{OC}), short-circuit current density (J_{SC}), and fill factor (FF). The photovoltaic performance of passivated individual NW and NW arrays was compared under 532 nm laser illumination with power density of $\sim$10 W/cm^2. Higher values of V_{OC} and FF in the NW arrays are explained by enhanced light trapping. In order to verify the effect of NW density on light absorption and hence on the photovoltaic performance of NW arrays, dense Si NW arrays were fabricated using nanoimprint lithography to periodically arrange the gold seed particles prior to epitaxial growth. Compared to sparse NW arrays fabricated using VLS growth from randomly distributed gold seeds, the nanoimprinted NW array solar cells show a greatly increased peak external quantum efficiency of $\sim$8% and internal quantum efficiency of $\sim$90% in the visible spectral range. Three-dimensional finite-difference time-domain simulations of Si NW periodic arrays with varying pitch (P) confirm the importance of high NW density. Specifically, due to diffractive scattering and light trapping, absorption efficiency close to 100% in the 400–650 nm spectral range is calculated for a Si NW array with P = 250 nm, significantly outperforming a blanket Si film of the same thickness. © *2015 AIP Publishing LLC*. [http://dx.doi.org/10.1063/1.4916535]

Metal-catalyzed vapor-liquid-solid (VLS) growth of Si/Ge axial *p-i-n* junction nanowires (NWs) is of interest because of their potential application for large-area, broad-spectrum, high-efficiency solar cells. It has recently been demonstrated that it is possible to grow Si/Ge axial hetero-junction NWs with abrupt interfaces,[1–3] as well as to control both Si and Ge composition and doping profiles.[4] This opens up new possibilities for solar cell devices. A promising possible structure is an array of hetero-NWs with separate *p-i-n* Ge and Si sections connected by a low-resistance *np* tunneling contact, leading to a solar cell with broader absorption, higher open-circuit voltage (V_{OC}), and higher overall efficiency compared to an all-Si NW solar cell. Investigation of such devices is still in its infancy. Before realizing this promising hetero-NW device, we focus here on the characterization of solar cells made from axial *p-i-n* Si NWs with diameters $\sim$100–200 nm.

Recent studies on Si NW solar cells were mostly focused on radial *p-n* or *p-i-n* junctions with relatively large wire diameters, between 1 and 20 μm, and array pitch (P) between 1 and 30 μm.[5–16] For example, in 2012, Gharghi *et al.*[11] reported a hetero-junction Si micro-wire solar cell with core/shell geometry and V_{OC} of 0.591 V, short-circuit current density (J_{SC}) of 31.1 mA/cm^2 and power conversion efficiency (PCE) of 12.2%. In 2013, Yoo *et al.*[14] demonstrated epitaxial growth of radial Si *p-i-n* junction solar cell with very high J_{SC} of 40 mA/cm^2 and 10.8% PCE despite a relatively low V_{OC} of 0.4 V. One of the main reasons that a radial geometry is preferred is that, in such a structure, the carrier separation takes place in the radial direction, so the carrier collection distance is smaller or comparable to the minority carrier diffusion length, resulting in a higher carrier collection efficiency. On the other hand, Si NW solar cells based on axial *p-n* or *p-i-n* junctions have received less attention. While there have been recent reports of axial NW cells based on InP (Ref. 17) and GaAs,[18] the most recent paper on axial Si *p-i-n* junction dates back to 2009, where Tian *et al.*[19] reported a single Si NW solar cell with V_{OC} = 0.29 V, short-circuit current I_{SC} = 31.1 pA, and PCE of 0.5% in a $\sim$300 nm diameter NW.

In this paper, we focus on truly sub-micrometer Si axial *p-i-n* junction NWs with diameter <200 nm. The axial geometry and smaller diameter are chosen in view of future realization of Si/Ge hetero-NWs, where the lattice mismatch strain can be alleviated by lateral sidewall expansion, which is impossible in a radial geometry. Moreover, unlike the radial geometry, an axial geometry allows the introduction of a long intrinsic section between the junctions, which effectively reduces the leakage current,[19] thus improving the ideality factor. Both sparse random NW arrays and dense square arrays with pitch P = 500 nm were studied, with the latter chosen based on a 3D finite-difference time-domain (FDTD) simulation of the optical properties for NW arrays of varying P, where it was found that a square periodic NW

array of sub-0.5 μm pitch—within reach of nanoimprint lithography (NIL)—would outperform a blanket Si *p-i-n* junction of the same thickness. The small P also allows us to achieve relatively large active area.

In all of our structures, vertical arrays of Si NWs were grown at 900 °C from $SiCl_4/H_2/N_2$ mixture using 100 nm Au nanoparticles randomly dispersed on 350 μm thick p^+-Si (111) substrates with doping of $\sim 10^{19}\,cm^{-3}$. We utilized BCl_3 (2% in N_2) and PH_3 (100 ppm in N_2) as the *p*- and *n*-type dopants, respectively, with B (P)/Si ratio in the gas phase of 3×10^{-3} (1.3×10^{-5}). In our sparse random NW arrays, the axial *p-i-n* junctions were formed by the sequential growth of 4 μm long B-doped, nominally undoped, and P-doped sections of NWs, for a total length $L \sim 12\,\mu m$. The total NW growth time was 6 min, with 2 min for each section. We did not observe any significant variations in the growth rate of Si NWs due to the dopants, which is presumably caused by low BCl_3 and PH_3 partial pressures as well as by the high growth rate of undoped Si NWs ($\approx 2.0 \pm 0.1\,\mu m/min$). The dopant densities of the *p*- and *n*-sections have a lower bound of $\sim 6 \times 10^{17}\,cm^{-3}$ from the two-point resistance measurements of individual NWs (assuming perfect contacts, the actual doping density is $>10^{18}\,cm^{-3}$ as estimated by STEM EELS analysis—not shown here), as well as from other Si NWs grown under the same conditions.

Figure 1(a) shows a tilted scanning electron microscope (SEM) image of a vertically aligned Si NW array. Different contrast in the SEM image taken at a higher magnification in Fig. 1(b) corresponds to the doping profile along the NW axis with the *p*-doped section being the brightest one.[20] The diffusion lengths of the dopants are less than 20 nm, taking the dopant diffusion coefficients on the order of $10^{-14}\,cm^2/s$,[21] and hence negligible compared to the length of intrinsic section. In an attempt to obtain a sharper doping profile, a 30 s growth interruption was adopted while switching the doping gases during which the hydrogen flow was reduced, so the growth rate of Si NWs was close to zero.[22] Figure 1(c) shows the transition between *p*-doped and undoped segments, which is marked by a small bulge caused by the growth interruption. In these arrays, the average NW density was relatively low, on the order of ~ 0.1–$0.2\,\mu m^{-2}$, as determined from top-view SEM images, resulting from the low Au nanoparticle surface density. The density can be enhanced significantly by turning to NIL, as will be discussed later.

After growth, passivation of Si NW surface was achieved by rapid thermal oxidation at 1000 °C for 1 min to form a SiO_2 sheath of $\sim$12 nm thickness.[23] Inset in Fig. 1(a) shows a transmission electron microscopy (TEM) image of an oxidized Si NW. The NW arrays were planarized using SU-8 photoresist,[24] followed by reactive ion etching (RIE) with CF_4:O_2 = 4:1 (Ref. 25) to expose the NW tips. Top contact electrodes to the *n*-doped NWs were made by sputter deposition of a 200 nm indium-zinc-oxide (IZO) layer that is transparent in the visible spectral range. The *p*-contact was made by backside metallization of the p^+-Si substrate with Ag paste. The number of NWs contacted together in the 2.5 mm diameter top electrode area of the unpassivated array (density $\approx 0.18\,\mu m^{-2}$) was about 9×10^5; for the passivated

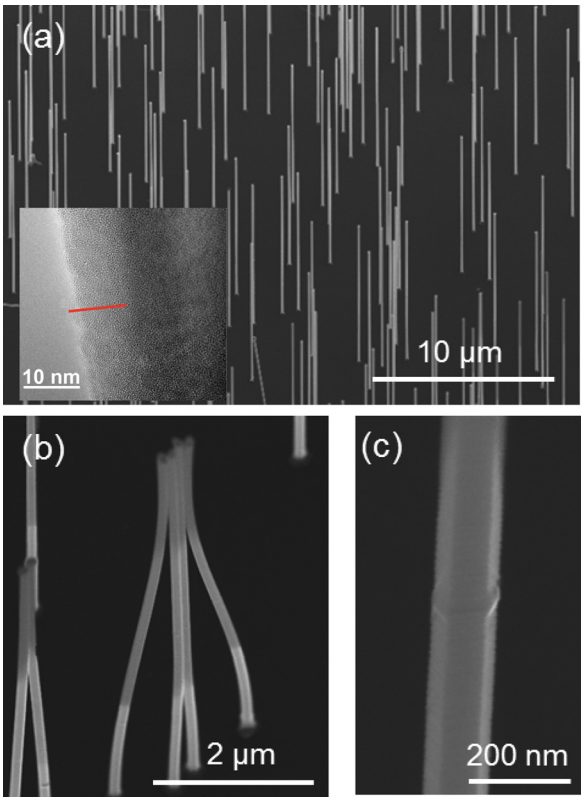

FIG. 1. *p-i-n* Si NWs grown from 100 nm Au nanoparticles: (a) and (b) 30 °-tilted view of the NW arrays. Contrast in (b) reveals the doping profile along the NW axis (due to charging effects, the initially isolated Si NWs collapsed under the e-beam upon SEM analysis); (c) small bulge on the NW trunk which forms during growth interruption. Inset in (a) shows a high-resolution TEM image of a passivated wire with a $\sim$12 nm SiO_2 sheath, indicated by the red marker.

array (density $\approx 0.09\,\mu m^{-2}$) with $0.8 \times 0.8\,mm^2$ top electrode area, the corresponding number was about 6×10^4, as estimated from top-view SEM micrographs.

Figure 2 shows the photovoltaic (PV) performance of both unpassivated and passivated Si NW arrays in dark and under AM 1.5 global (G) illumination. Clear rectification behavior and power generation were observed in both arrays. The unpassivated Si NW arrays in Fig. 2(a) exhibited an open circuit voltage $V_{OC} = 170$ mV, a short circuit current density $J_{SC} > 10.5\,\mu A/cm^2$ (with some uncertainty due to the unknown fraction of properly contacted NWs), and a fill factor FF = 30%.

It is evident from the *I-V* curve that the unpassivated array in Fig. 2(a) has a relatively high series resistance and low shunt resistance. In the NW arrays passivated by rapid thermal oxidation[26] in Fig. 2(b), the performance is improved, with V_{OC} and FF increasing to 250 mV and 36%, respectively. The seemingly lower J_{SC} in the passivated NW array of Fig. 2(b) is due to a lower NW density. A more proper comparison of the current density calculated by considering the cross-sectional area of the Si NWs only, rather than the total electrode area, would give $J_{NW} > 3.7\,mA/cm^2$ for unpassivated array and $J_{NW} > 6.5\,mA/cm^2$ for the passivated one. The clear improvements in V_{OC} and J_{SC} are consistent with the expected reduction in the surface recombination rate.[27] It should be pointed out that the NWs

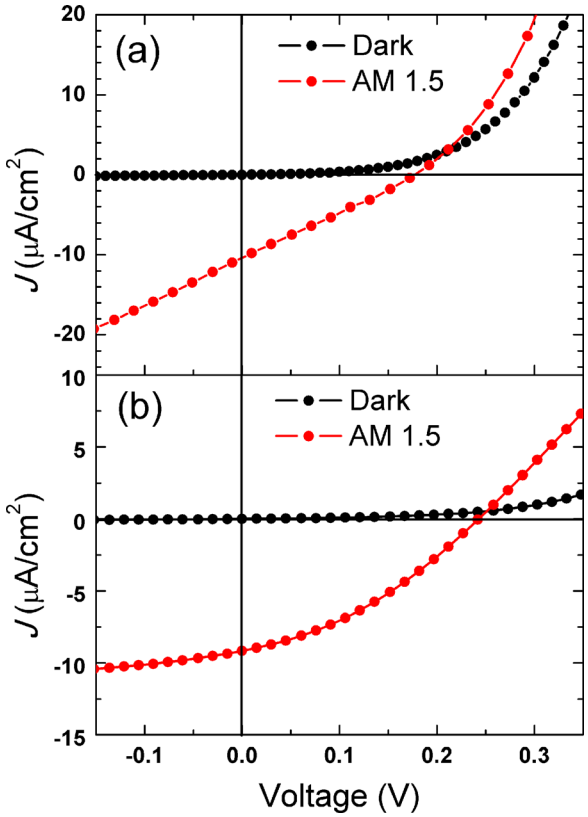

FIG. 2. Photovoltaic performance of the Si NW array solar cell under AM 1.5G illumination: (a) unpassivated, (b) passivated with 12 nm thermal SiO_2. Due to its lower NW density, J_{SC} is lower in the passivated NW array, but is in fact higher if we consider the cross-sectional area of the Si NWs only. See text for details.

in the passivated array had a slightly smaller diameter due to the consumption of Si during thermal oxidation (see inset of Fig. 1), implying better PV performance even with smaller light-absorbing Si volume.

As a proof of the improved surface conditions of the passivated samples, we measured the response time of both passivated and unpassivated samples. For the measurement set up, the samples were illuminated by a 640 nm laser beam with a square wave output. The samples were not biased by external sources and were connected to a 4.5 kΩ resistor load. We monitor the photocurrent generated in the device through the resistor using an oscilloscope. Figure 3 shows the results (for clarity, the signals are normalized). The exponential fitting coefficients for the unpassivated and passivated samples are 0.36 μs and 0.55 μs, respectively. The passivated sample shows a ~50% longer response time. For comparison, we also measured the response time of a high-efficiency reference single-crystalline Si solar cell, which exhibits a much longer response time, due to optimized passivation, see Fig. 3.

Compared to planar devices, NW solar cell devices are expected to exhibit improved optical characteristics.[28–30] We have performed reflectivity measurements using an integrating sphere coupled to the external quantum efficiency (EQE) measurement system (QEX10, PV Measurements, Inc.) where a calibration sample was used as the reflectance standard (Fluorilon FWS-99-10 c, Avian Technologies).[31] The

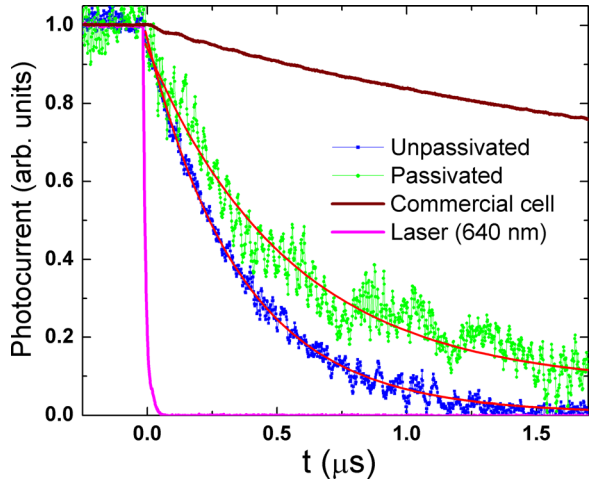

FIG. 3. Measured response times of passivated and unpassivated samples, together with the laser pulse shape. The solid red lines are the fitting curves with fitting coefficients equal to 0.36 μs and 0.55 μs for unpassivated and passivated samples, respectively. For comparison, a reference single-crystalline Si solar cell with optimized passivation is also plotted.

measured reflectance spectra are shown in Fig. 4. We observed a total reflectance (including specular and diffuse components) of ~20% over the 400–1100 nm spectral range, which is significantly lower than that of a planar device with no anti-reflection coating, implying less reflectance loss and more light trapping. The fact that the overall reflectance of the passivated sample is slightly higher than the unpassivated one is due to lower NW density (0.09 μm^{-2} as compared to 0.18 μm^{-2} for the unpassivated sample). It is interesting to note that the measured specular reflectance of the planarized NW array was ~6% (dotted green line in Fig. 4), indicating strong light scattering by the NWs.

To further prove that the NW devices can benefit from the array structure leading to enhanced absorbance, the PV performance of individual NWs and NW arrays passivated under the same conditions was compared using a 532 nm laser with a power density of 10 W/cm^2 (a laser was used

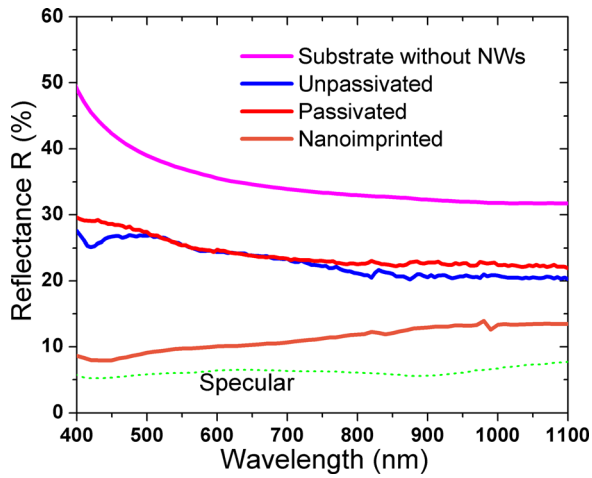

FIG. 4. Measured reflectance of the solar cell samples after SU-8 planarization. Very low normal specular reflectance (green dotted line) of ~6% indicates strong light scattering by the NWs. The reflectance of a nanoimprinted sample (sample B, will be discussed later) with much higher NW density is also shown for comparison.

here because the AM 1.5G response of the individual NW was too weak to be measured). Note that an individual horizontally aligned NW cannot be directly compared to a vertical NW array, since the active region of the individual NW is exposed to the full optical field of the laser, whereas in a vertical NW array, there is optical loss in the *n*-contact regions above the active regions of the NWs (especially at shorter wavelengths). Nonetheless, the NW array sample exhibits improved V_{OC} and FF compared to the individual NW (Fig. 5), which can be assigned to enhanced light trapping in the NW arrays. It should be also noted that compared with the NW array devices, we have introduced more series resistance for the single NW device by making an extra metal (Ni) contact to the *p*-Si (inset in Fig. 5(a)), however contact series resistance should have no impact on V_{OC}.

While the passivated sample showed improved V_{OC}, J_{SC}, and FF, the EQE is low (<1%) for both unpassivated and passivated samples (Fig. 6(a)). The best way to understand this is to carry out the optical FDTD simulations. There have been numerous reports on optimizing absorption of nanowire arrays.[32–34] However, their conclusions vary since the absorption is driven by numerous competing factors and most of the studies focus on different parameters, such as radii,[32,34] length,[32,33] and pitch.[34] Here, we study the effect of NW pitch and length on the absorption while keeping the NW diameter constant (consistent with our VLS growth). Figure 6(b) reports the simulated optical absorption

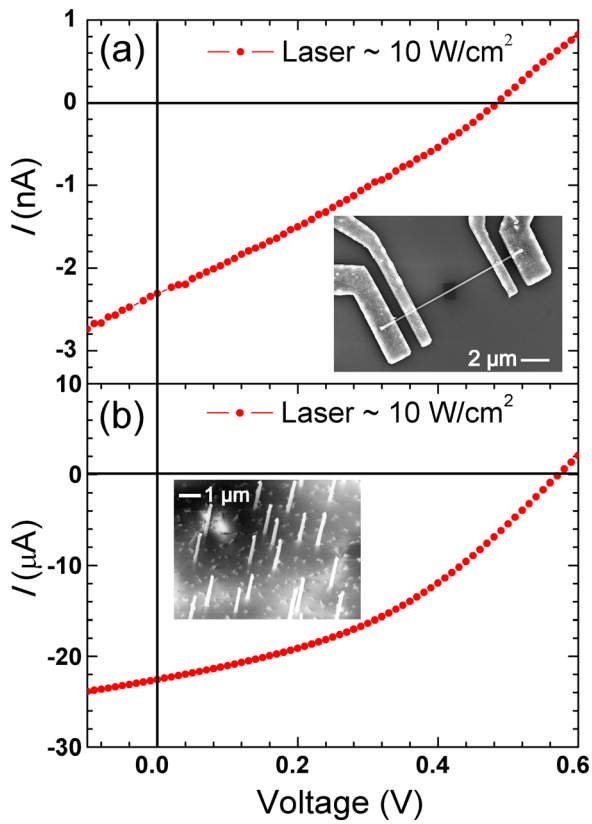

FIG. 5. Comparison under 532 nm laser illumination of a single Si NW (a) with $V_{OC} = 0.49$ V, FF = 28.3% and a passivated Si NW array (b) with $V_{OC} = 0.58$ V, FF = 39.3%. Insets show the four-point *I-V* measurement geometry of the single NW (a) and a top view SEM of the planarized array with the protruding NW tips clearly visible (b).

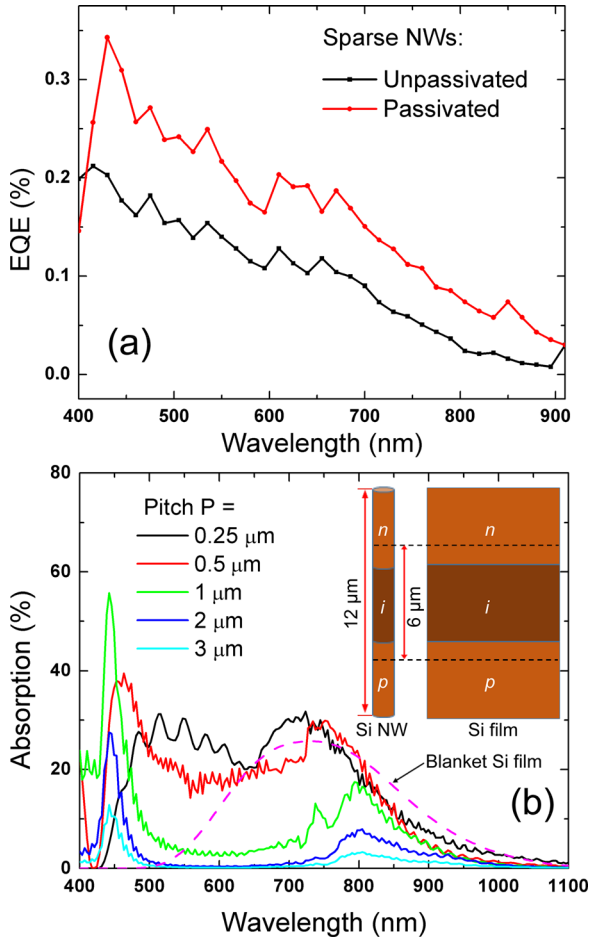

FIG. 6. (a) EQE of both passivated and unpassivated NW arrays; (b) FDTD simulated absorption spectra of the active region in square NW arrays (12 μm long NWs of 140 nm diameter and 4 μm intrinsic section) as a function of P. The absorption spectrum of a 12 μm thick Si film with the same doping profile is plotted for comparison, see inset for simulation geometry.

as extracted from a full 3D FDTD simulation, for *n-i-p* NW arrays with P ranging from 0.25 μm to 3 μm and considering an active region comprising the intrinsic 4 μm section and estimated 1 μm minority carrier diffusion lengths in both *p*-type and *n*-type doped sections (see insets in Fig. 6(b) for the simulation geometry, including the blanket Si film of the same doping for comparison). The assumption is that electron-hole (*e–h*) pairs photo-generated in the active region will contribute to the observed photocurrent, while *e–h* pairs generated in the highly doped regions will suffer Auger recombination and not contribute significantly to the photocurrent. The Si NW length and diameter were set to the experimentally determined values of 12 μm and 140 nm, respectively. The 12 nm thickness of SiO_2 was not taken into consideration since it is sufficiently thin not to affect the optical reflection in the 400–1100 nm wavelength range. The total height of the simulated region (along the NW axis) was set to be 14.5 μm long in order to enclose the full NW length and also extend into the underlying silicon substrate. Perfectly matched layer (PML) boundary conditions were used to prevent spurious reflections. A plane wave injection source was located directly above the NW array. Power monitors were placed at different positions to record the power

flow at different heights along the NW array axis, so that absorption for different sections of the NW array could be calculated from the difference of the power flow between corresponding monitors. During the simulation, non-uniform mesh was used with roughly 15 mesh points per wavelength (in the medium), which balanced accuracy and computational cost. In order to minimize the simulation volume and runtime, the NW arrays were assumed to be uniform and distributed according to a square lattice, so that periodic boundary conditions could be imposed on the remaining lateral dimensions. Also, the NWs were embedded in 10 μm thick SU-8 photoresist, with index of refraction taken from Ref. 35. For the NWs, we used the Si refractive index as reported by Palik.[36]

As can be seen in Fig. 6(b), in a sparse array with period $P = 3\ \mu m$, which is close to the average inter-wire distance in our random NW arrays, a strong absorption peak can be observed at shorter wavelengths near $\lambda = 450$ nm. The absorption peak becomes stronger at $P = 1\ \mu m$, and then weakens and merges into the absorption spectrum for denser arrays ($P \leq 0.5\ \mu m$). By comparison, due to the large absorption coefficient of Si at shorter wavelengths (e.g., $\alpha = 2.55 \times 10^4\ cm^{-1}$ at 450 nm, corresponding to a propagation length of 390 nm), a blanket Si film with same total thickness of 12 μm (and same substrate) shows no significant absorption in the 6-μm-thick middle active region for $\lambda < 550$ nm, since most of the incident light is absorbed in the top region. Thus, the NW arrays perform better since diffractive scattering from each sub-micron diameter NW allows for a significant fraction of the incident electromagnetic fields to be directed off-normal and reach the active regions of neighboring NWs.

In order to experimentally verify our simulation results, dense Si NW square arrays with $P = 0.5\ \mu m$ were fabricated using NIL technique to arrange the gold seed particles. MR-I 7020E resist was first spun on a heavily p-doped Si (111) substrate. A mold with an array of 150-nm-diameter pillars and P = 500 nm was then pressed into the resist, followed by RIE to remove the residue and expose the Si substrate. Thereafter, 30 nm of Au was evaporated on the substrate and the polymer was lifted-off in acetone (see Fig. 7(a)), leaving behind a periodic array of gold nanodots. Figure 7(b) shows the resulting square array of gold seed particles. The NWs growth, SiO_2-passivation, and device fabrication were identical to the random Si NW arrays reported above. The resulting *p-i-n* NW segments were 1.7 μm, 3.5 μm, 1.7 μm (sample A, total NW length $L \sim 7\ \mu m$) and 2.2 μm, 5 μm, and 1.6 μm (sample B, $L \sim 8.8\ \mu m$). The NW diameter was ~170 nm for both samples. The slightly larger NW diameter is due to larger gold seed particles formed by NIL. Figure 7(c) shows a top view of sample A. It can be seen that some NWs are missing or merged during the growth, resulting in a lower NW density ($\sim 2\ \mu m^{-2}$ for both samples) than the nanoimprint maximum ($4\ \mu m^{-2}$). Figure 7(d) shows a 52 °-tilted view of a NW array after IZO deposition, with contacted NWs poking through the IZO.

The photovoltaic characterization of samples A and B is reported in Figs. 8 and 9. It is evident from Fig. 9(a) that the EQE increased by more than one order of magnitude to peak

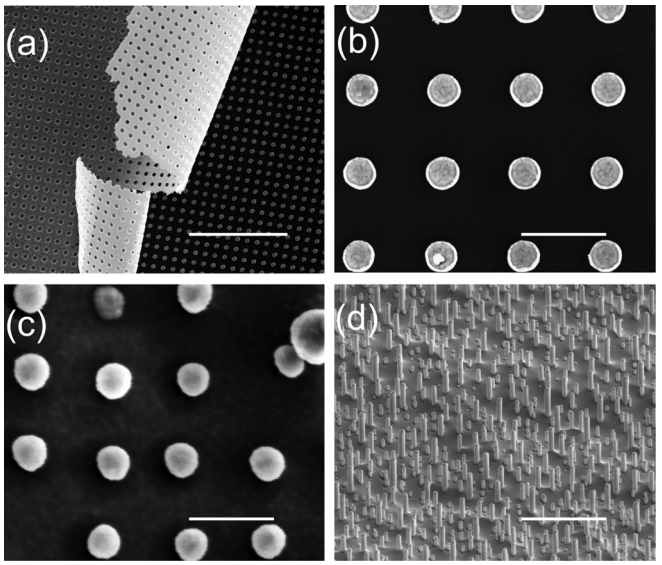

FIG. 7. Nanoimprint lithography for dense NW array growth: (a) MR-I 7020E resist lift-off, leaving behind a square array of 30 nm thick gold particles; (b) close-up of NIL-arranged gold seed particles with P = 500 nm and diameter of ~150 nm; (c) top-view of NW array, with some NWs missing or merged during the growth, resulting in a lower final NW density than the nanoimprint maximum; (d) 52 °-tilted view of NW array after IZO top contact deposition. Scale bars are 5 μm for (a) and (d) and 500 nm for (b) and (c).

values of about 3% at 500 nm (Sample A) and 8% at 570 nm (Sample B). Sample B exhibited better performance than sample A as a result of higher absorption due to longer NWs, indicating the possibility of a further improvement by using even longer NWs (as discussed later). The corresponding FDTD-simulated absorption spectra are shown in Fig. 9(b), where the simulation geometry consisting of a square array of NWs with an active region comprising the intrinsic sections plus 1 μm excursions into the *p*- and *n*-type doped sections, as shown in the insets of Fig. 9(b). We can further extract the internal quantum efficiency (IQE) from the EQE spectra by dividing the experimentally measured EQE by the

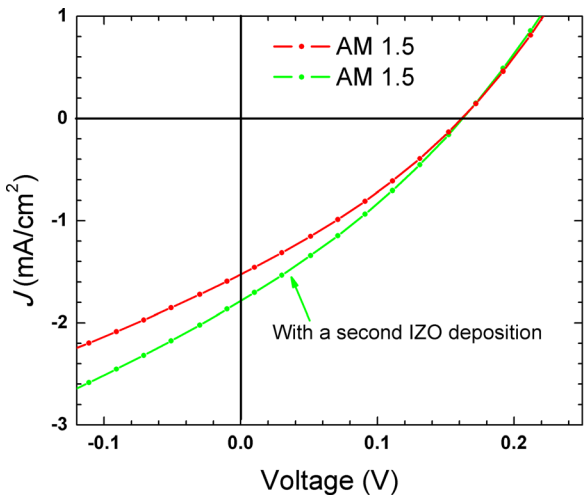

FIG. 8. Photovoltaic performance of sample B under AM 1.5G illumination. The green dashed line shows a 15% improvement on J_{SC} after a second deposition of IZO top contact with the sample tilted at a small angle with respect to the IZO source.

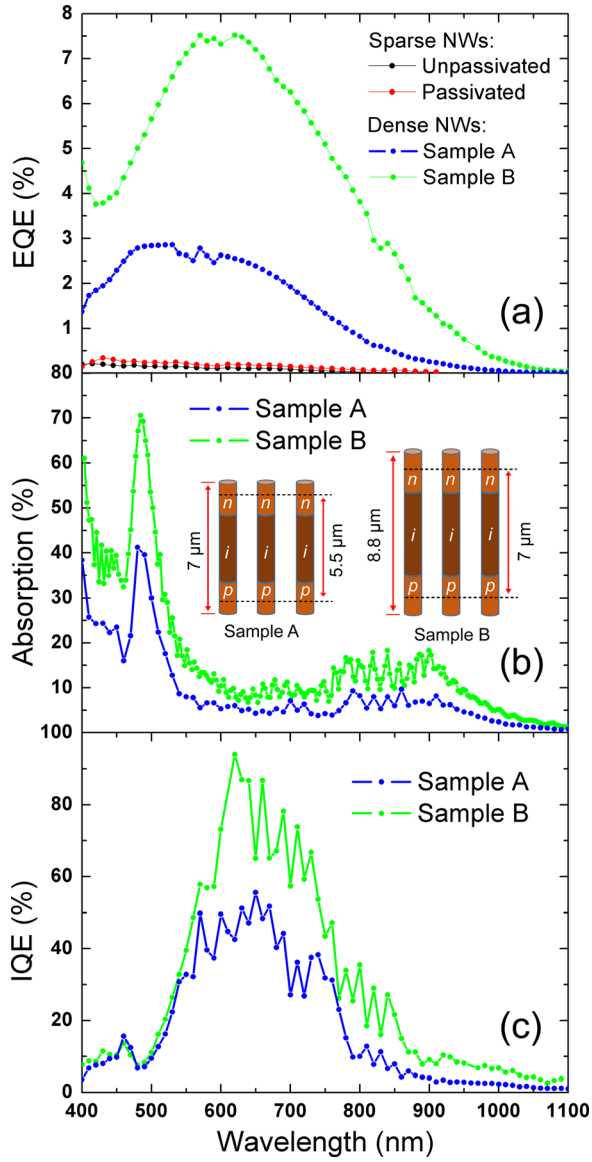

FIG. 9. (a) Experimental EQE of dense square NW arrays produced by NIL with same pitch P = 500 nm and NW lengths of 7 μm (sample A) and 8.8 μm (sample B), respectively; the EQE dependences for sparse NW arrays of Fig. 6(a) are also plotted for comparison; (b) simulated (FDTD) absorption spectra of the active region (5.5 and 7 μm) of the dense square NW arrays; (c) calculated IQE of the dense square NW arrays.

simulated absorption. The result, shown in Fig. 9(c), gives a peak IQE of ~50% (sample A) and 90% (sample B) in the visible range for our dense nanoimprinted NW arrays.

It should be noted that the absorption calculated in Fig. 9(b) is relatively low, due to the relatively short NWs used in the NIL-produced array growth (total NW length $L \sim 7$ and 8.8 μm for samples A and B, respectively). The absorption can be further enhanced by using longer NWs with longer intrinsic sections and shorter doped electrodes.

Several features of our NW arrays still require optimization to improve the PV performance. First, while the passivation step helped increase the recombination time, V_{OC} and J_{SC} are still rather low. One possible reason would be the NWs are still suffering from the high surface recombination velocity (SRV), since the axial structure of our device is very sensitive to SRV due to the exposed depletion region at

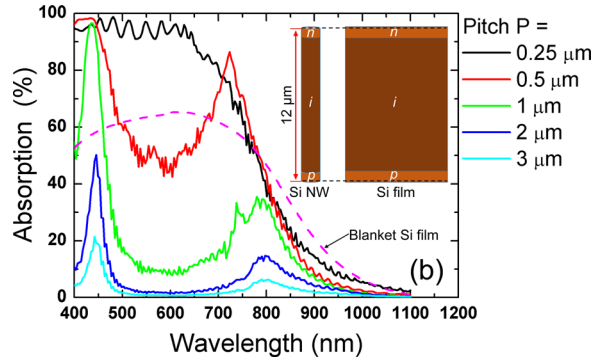

FIG. 10. Simulated light absorption in optimized NW arrays with a large ~11 μm intrinsic region and thin doped electrodes, compared to blanket Si.

the surface.[37] Another possibility that would lead to a low J_{SC} is that not all the nanowires were properly contacted. In fact, the green dashed line in Fig. 8 shows a 15% improvement on J_{SC} after a second deposition of IZO top contact with the sample tilted at a small angle with respect to the IZO source, ensuring a higher fraction of contacted NWs. Second, since carrier separation is most efficient within the depletion region,[38] the *p*- and *n*-sections of the NWs should be made shorter and the *i*-Si section should be made longer to improve the carrier collection efficiency. To verify this, we repeated the 3D FDTD simulations for arrays of NWs with the same total length $L \sim 12$ μm as in Fig. 6(b) but with much shorter doped electrodes (see inset in Fig. 10 for the new NW geometry). As can be seen in Fig. 10, the absorption, integrated over the entire 12 μm length, is low when P ≥ 2 μm, with the overall absorption of the NW arrays lower than that of a blanket Si film. The physical reason for this result is that most of the incident light propagates and is absorbed directly in the silicon substrate, thus explaining the low experimental reflectance, as shown in Fig. 4, and low EQE. Moreover, the diffracted propagating modes generated by the presence of NWs increase the transmission into the Si substrate, further reducing the reflectance and optical absorption in the NW array.[31] However, as the density of the NWs increases, the simulated absorption of the NW arrays does as well, exceeding the absorption of a blanket Si film when P ≤ 0.5 μm and also improving on the previous structure with 4 μm long *p*-, *n*- and *i*-sections. Finally, increasing the NW density by reducing P well below 0.5 μm can further improve the performance. For example, according to our simulations in Fig. 10, the absorption reaches nearly unity for $\lambda < 700$ nm when P = 0.25 μm. A cell with improved performance will also have to rely on uniformly contacted NWs to increase the carrier extraction efficiency over the entire area.

In summary, we have demonstrated solar cells based on Si axial *p-i-n* junction NW arrays with diameter <200 nm. We have studied the PV performance of both unpassivated and SiO_2-passivated samples under AM 1.5 G illumination. The improvements on recombination time, V_{OC}, J_{SC}, and FF for passivated samples were explained by reduced surface recombination. The enhanced optical characteristics of our NW arrays devices were confirmed by reflectance measurements, as well as the comparison of PV performance of

passivated Si NW arrays and single NW devices. Dense Si NW arrays were fabricated using NIL. Improved EQE of ~3% and 8% and peak IQE of ~ 50% and 90% in the visible spectral range were obtained for samples with different NW lengths, due to improved absorption, according to FDTD simulations of absorption in Si NW arrays with varying pitch. We believe that the performance of our NW solar cells could be further improved by optimizing the geometry of the NW and by increasing the NW density. The study of Si axial *p-i-n* junction NW solar cells provides a promising alternative for PV applications of Si and sheds light on the realization of high performance NW tandem solar cells.

The work at Brown University was supported by the National Science Foundation Award Nos. ECCS-1068895 and DMR-1203186. The University of Maryland portion of the work was partially supported by the National Science Foundation under Grant No. ECCS-0112802. We thank Dr. Vladimir P. Oleshko of MML/NIST for providing the TEM images of oxidized Si nanowires.

[1]D. E. Perea, N. Li, R. M. Dickerson, A. Misra, and S. T. Picraux, "Controlling heterojunction abruptness in VLS-grown semiconductor nanowires via in situ catalyst alloying," Nano Lett. **11**, 3117 (2011).
[2]J. L. Lensch-Falk, E. R. Hemesath, D. E. Perea, and L. J. Lauhon, "Alternative catalysts for VSS growth of silicon and germanium nanowires," J. Mater. Chem. **19**, 849 (2009).
[3]C. Y. Wen, M. C. Reuter, J. Bruley, J. Tersoff, S. Kodambaka, E. A. Stach, and F. M. Ross, "Formation of compositionally abrupt axial heterojunction in silicon-germanium nanowires," Science **326**, 1247 (2009).
[4]D. E. Perea, D. K. Schreiber, A. Devaraj, T. Thevuthasan, J. Yoo, S. A. Dayeh, and S. T. Picraux, "Controlling axial p-n heterojunction abruptness through catalyst alloying in vapor-liquid-solid grown semiconductor nanowires (Poster Abstract)," in Microscopy and Microanalysis Conference, Phoenix, AZ, 29 July–2 August 2012.
[5]L. Tsakalakos, J. Balch, J. Fronheiser, and B. A. Korevaar, "Silicon nanowire solar cells," Appl. Phys. Lett. **91**, 233117 (2007).
[6]M. C. Putnam, S. W. Boettcher, M. D. Kelzenberg, D. B. Turne-Evans, J. M. Spurgeon, E. L. Warren, R. M. Briggs, N. S. Lewis, and H. A. Atwater, "Si microwire-array solar cells," Energy Environ. Sci. **3**, 1037–1041 (2010).
[7]O. Gunawan, K. Wang, B. Fallahazad, Y. Zhang, E. Tutuc, and S. Guha, "High performance wire-array silicon solar cells," Prog. Photovoltaics: Res. Appl. **19**, 307–312 (2011).
[8]C. E. Kendrick, H. P. Yoon, Y. A. Yuwen, G. D. Barber, H. Shen, T. E. Mallouk, E. C. Dickey, T. S. Mayer, and J. M. Redwing, "Radial junction silicon wire array solar cells fabricated by gold-catalyzed vapor-liquid-solid growth," Appl. Phys. Lett. **97**, 143108 (2010).
[9]D. R. Kim, C. H. Lee, P. M. Rao, I. S. Cho, and X. Zheng, "Hybrid Si microwire and planar solar cells: passivation and characterization," Nano Lett. **11**, 2704–2708 (2011).
[10]G. Jia, M. Steglich, I. Sill, and F. Falk, "Core-shell heterojunction solar cells on silicon nanowire arrays," Sol. Energy Mater. Sol. Cells **96**, 226–230 (2012).
[11]M. Gharghi, E. Fathi, B. Kante, S. Sivoththaman, and X. Zhang, "Heterojunction silicon microwire solar cells," Nano. Lett. **12**, 6278–6282 (2012).
[12]L. Yu, L. Rigutti, M. Tchernycheva, S. Misra, M. Foldyna, G. Picardi, and P. R. i Cabarrocas, "Assessing individual radial junction solar cells over millions on VLS-grown silicon nanowires," Nanotechnology **24**, 275401 (2013).
[13]K. Seo, J. J. Yu, P. Duane, W. Zhu, H. Park, M. Wober, and K. B. Crozier, "Si microwire solar cells: Improved efficiency with a conformal SiO_2 layer," ACS Nano **7**, 5539–5545 (2013).
[14]J. Yoo, S. A. Dayeh, W. Tang, and S. T. Picraux, "Epitaxial growth of radial Si *p-i-n* junctions for photovoltaic applications," Appl. Phys. Lett. **102**, 093113 (2013).
[15]D. Kohen, C. Morin, P. Faucherand, A. Brioude, and S. Perraud, "Enhanced photovoltaic performance of vapor-liquid-solid grown silicon nanowire array with radial heterojunction," Phys. Status Solidi A **211**, 1143–1149 (2014).
[16]G. Jia, A. Gawlik, J. Bergmann, B. Eisenhawer, S. Schönherr, G. Andrä, and F. Falk, "Silicon nanowire solar cells with radial p-n heterojunction on crystalline silicon thin films: Light trapping properties," IEEE J. Photovoltaics **4**, 28–32 (2014).
[17]J. Wallentin, N. Anttu, D. Asoli, M. Huffman, I. Åberg, M. H. Magnusson, G. Siefer, P. Fuss-Kailuweit, F. Dimroth, B. Witzigmann, H. Q. Xu, L. Samuelson, K. Deppert, and M. T. Borgström, "InP nanowire array solar cells achieving 13.8% efficiency by exceeding the ray optics limit," Science **339**, 1057 (2013).
[18]M. Yao, N. Huang, S. Cong, C. Chi, M. A. Seyedi, Y. Lin, Y. Cao, M. L. Povinelli, P. D. Dapkus, and C. Zhou, "GaAs nanowire array solar cells with axial *p-i-n* juncitons," Nano Lett. **14**, 3293–3303 (2014).
[19]B. Tian, T. J. Kempa, and C. M. Lieber, "Single nanowire photovoltaics," Chem. Soc. Rev. **38**, 16–24 (2009).
[20]D. D. Perivic, M. R. Castell, A. Howie, C. Lavoie, T. Tiedje, and J. S. W. Cole, "Field-emission SEM imaging of compositional and doping layer semiconductor superlattices," Ultramicroscopy **58**, 104 (1995).
[21]N. R. Zangenberg, J. Fage-Pedersen, J. L. Hansen, and A. N. Larsen, "Boron and phosphorus diffusion in strained and relaxed Si and SiGe," J. Appl. Phys. **94**, 3883 (2003).
[22]S. Krylyuk, A. V. Davydov, and I. Levin, "Tapering control of Si nanowires grown from $SiCl_4$ at reduced pressure," ACS Nano **5**, 656 (2011).
[23]S. Krylyuk, A. V. Davydov, I. Levin, A. Motayed, and M. Vaudin, "Rapid thermal oxidation of silicon nanowires," Appl. Phys. Lett. **94**, 063113 (2009).
[24]A. C. E. Chia and R. R. LaPierre, "Contact planarization of ensemble nanowires," Nanotechnology **22**, 245304 (2011).
[25]P. M. Dentinger, W. M. Clift, and S. H. Goods, "Removal of SU-8 photoresist for thick film applications," Microelectron. Eng. **61–62**, 993–1000 (2002).
[26]A. G. Aberle, S. W. Glunz, A. W. Stephens, and M. A. Green, "High-efficiency silicon solar cells: Si/SiO_2, interface parameters and their impact on device performance," Prog. Photovoltaics: Res. Appl. **2**, 265–273 (1994).
[27]A. D. Mohite, D. E. Perea, S. Singh, S. A. Dayeh, I. H. Campbell, S. T. Picraux, and H. Htoon, "Highly efficient charge separation and collection across in situ doped axial VLS-grown Si nanowire p−n junctions," Nano Lett. **12**, 1965–1971 (2012).
[28]L. Hu and G. Chen, "Analysis of optical absorption in silicon nanowire arrays for photovoltaic applications," Nano Lett. **7**, 3249–3252 (2007).
[29]E. Garnett and P. Yang, "Light trapping in silicon nanowire solar cells," Nano Lett. **10**, 1082–1087 (2010).
[30]K. Peng and S. T. Lee, "Silicon nanowires for photovoltaic solar energy conversion," Adv. Mater. **23**, 198–215 (2011).
[31]Certain commercial equipment instruments or materials are identified in this paper to foster understanding. Such identification does not imply recommendation or endorsement by the National Institute of Standards and Technology nor does it imply that the materials or equipment identified are necessarily the best available for the purpose.
[32]H. Alaeian, A. C. Atre, and J. A. Dionne, "Optimized light absorption in Si wire array solar cells," J. Opt. **14**, 024006 (2012).
[33]N. Huang, C. Lin, and M. L. Povinelli, "Broadband absorption of semiconductor nanowire arrays for photovoltaic applications," J. Opt. **14**, 024004 (2012).
[34]B. C. P. Sturmberg, K. B. Dossou, L. C. Botten, A. A. Asatryan, C. G. Poulton, R. C. McPhedran, and C. M. de Sterke, "Optimizing photovoltaic charge generation of nanowire arrays: a simple semi-analytic approach," ACS Photonics **1**, 683–689(2014).
[35]See www.microchem.com/RequestInformation.htm for data sheet for the refractive index of SU-8.
[36]E. D. Palik, *Handbook of Optical Constants of Solids* (Academic Press, 1985).
[37]J. D. Christesen, X. Zhang, C. W. Pinion, T. A. Celano, C. J. Flynn, and J. F. Cahoon, "Design principles for photovoltaic devices based on Si nanowires with axial or radial *p-n* junction," Nano Lett. **12**, 6024–6029 (2012).
[38]S. M. Sze, *Physics of Semiconductor Devices*, 2nd ed. (Wiley, 2004).